

Whole-system ultrasound resonances as the basis for acoustophoresis in all-polymer microfluidic devices

Rayisa P. Moiseyenko* and Henrik Bruus†

Department of Physics, Technical University of Denmark,
DTU Physics Building 309, DK-2800 Kongens Lyngby, Denmark

(Dated: 13 September 2018)

Using a previously well-tested numerical model, we demonstrate theoretically that good acoustophoresis can be obtained in a microchannel embedded in an acoustically soft, all-polymer chip, by excitation of whole-system ultrasound resonances. In contrast to conventional techniques based on a standing bulk acoustic wave inside a liquid-filled microchannel embedded in an elastic, acoustically hard material, such as glass or silicon, the proposed whole-system resonance does not need a high acoustic contrast between the liquid and surrounding solid. Instead, it relies on the very high acoustic contrast between the solid and the surrounding air. In microchannels of usual dimensions, we demonstrate the existence of whole-system resonances in an all-polymer device, which support acoustophoresis of a quality fully comparable to that of a conventional hard-walled system. Our results open up for using cheap and easily processable polymers in a controlled manner to design and fabricate microfluidic devices for single-use acoustophoresis.

I. INTRODUCTION

A steadily increasing number of papers report successful applications of ultrasound-based microscale acoustofluidic devices in biology, environmental and forensic sciences, and clinical diagnostics [1–5]. Examples include cell synchronization [6], enrichment of prostate cancer cells in blood [7], high-throughput cytometry and multiple-cell handling [8, 9], single-cell patterning and manipulation [10, 11], size-independent sorting of cells [12], and rapid sepsis diagnostics by detection of bacteria in blood [13]. Acoustics have also been used for non-contact microfluidic trapping and particle enrichment [14], massively parallel force microscopy on biomolecules [15], as well as acoustic tweezing [16–19].

In all applications, an appropriate magnitude of the acoustic forces is reached by resonant actuation of ultrasound waves, using one of two basic methods. One method relies on bulk acoustic waves (BAW), see Fig. 1(a), for which resonant modes are built up in liquid-filled acoustic resonators, say microchannels or microcavities, embedded in acoustically hard material such as silicon, glass and/or metal. For this method to work, it is crucial that the acoustic contrast between the liquid and the surrounding solid is sufficiently large, typically around 10 in terms of the acoustic impedance ratio. The other method relies on surface acoustic waves (SAW), Fig. 1(b), that are resonantly excited by using appropriately spaced interdigitated metallic transducer electrodes positioned on the surface of a piezoelectric substrate. For this method to work, it is crucial that the piezoelectric coupling constant of the substrate is sufficiently strong, and thus a popular choice is lithium niobate substrates, well-known from conventional electromechanical filters in

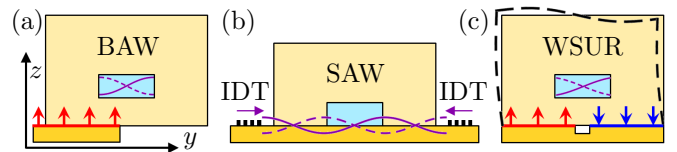


FIG. 1. Sketches of the conventional and proposed acoustophoresis techniques for a liquid-filled microchannel (blue) embedded in an elastic solid (beige). (a) Bulk acoustic waves (BAW) excited by a single piezo actuator (orange). (b) Surface acoustic waves (SAW) excited by interdigital transducers (IDT, black) on a piezoelectric substrate (orange). (c) The proposed whole-system ultrasound resonances (WSUR) excited by two piezo actuators excited in anti-phase (red and blue arrows). Magenta and dashed black curves represent pressure and displacement fields.

microwave technology. Both methods are actively being used in contemporary acoustofluidics as is evident from the following examples published in the literature the past two years. BAW devices have been used for cell focusing in simple and inexpensive aluminum devices [20], for binary particle separation in droplet microfluidics [21], for hematocrit determination [22], for enrichment of tumor cells from blood [23], and for manipulation of *C. elegans* [24, 25], while SAW devices have been used for nanoparticle separation [26, 27], for self-aligned particle focusing and patterning [28], for enhanced cell sorting [29], and for in-droplet microparticle separation [30].

Currently, the acoustofluidic devices with the highest throughput are of the BAW type [5]. However, a limiting factor for fully exploiting the application potential of such devices, is the cost of the glass or silicon components, used because of their high acoustic contrast relative to water. This limitation is especially severe for applications intended for point-of-care clinical use [3], where the acoustic separation unit must be a single-use consumable. This important problem could be overcome by using all-polymer microfluidic devices, if they could

* raymoi@fysik.dtu.dk

† bruus@fysik.dtu.dk

be made compatible with ultrasound acoustics, because that would allow for cheap conventional volume fabrication [31]. However, partly due to the lack of good theoretical understanding, it has proven difficult to make good all-polymer BAW-devices for acoustofluidics. But a few results for such devices have been published, including focusing of polymer beads [32–35], lipids [32], and red blood cells [33, 36], as well as blood-bacteria separation [37] and purification of lymphocytes [38].

The main goal of this work, is to provide a theoretical framework for designing all-polymer microfluidic devices capable of successful acoustophoretic applications. The structure of the paper is as follows: In Section II, we present the basic device geometry and the material properties. In Section III, we give a short overview of the theory of linear acoustics of the solid and the fluid, the acoustic radiation force on suspended tracer microparticles, and the numerical implementation of the model. The results of the numerical simulation for a simplified model in two dimensions (2D) of a conventional silicon-glass system are shown and analyzed in Section IV. They serve as a baseline for the 2D simulation results of an all-polymer device presented in Section V, where the principle of whole-system ultrasound resonances (WSUR), see Fig. 1(c), is established as a method to identify specific resonances suitable for successful acoustophoresis in this acoustically soft system. In Section VI, we present the results of a more realistic model in three dimensions (3D) of the all-polymer device, and discuss them in relation to preliminary experimental results. Finally, in Section VII, we summarize and discuss the obtained results.

II. GEOMETRY AND MATERIALS

Generic, mm-long, straight channels that are placed along the horizontal x axis and have a constant rectangular cross section in the vertical y - z plane, have been intensively studied in the literature both theoretically [39–42]

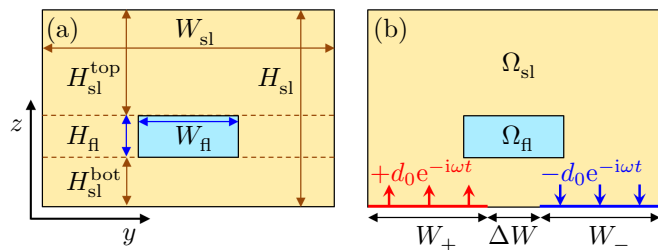


FIG. 2. (a) The vertical cross section in the y - z plane of the long, straight device. The elastic solid (beige, Ω_{sl}) has the outer widths W_{sl} and height H_{sl} , while the fluid channel (light blue, Ω_{fl}) has the width $W_{\text{fl}} = 377 \mu\text{m}$ and height $H_{\text{fl}} = 157 \mu\text{m}$. (b) A sketch of the anti-symmetric actuation $\mathbf{u}(W_{\pm}) = \pm d_0 e^{-i\omega t} \mathbf{n}$ of the time-harmonic displacement at the actuation regions W_+ (red) and W_- (blue) separated by the gap ΔW .

TABLE I. Material parameters at 25 °C for selected solids. The specific acoustic impedance is $Z_{\text{sl}} = \sqrt{\rho_{\text{sl}} C_{11}}$, and for isotropic materials $C_{12} = C_{11} - 2C_{44}$ (PMMA and Pyrex).

Parameter	Symbol	PMMA [47–52]	Pyrex [53]	Si [54]	Unit
Mass density	ρ_{sl}	1190	2230	2329	kg m^{-3}
Elastic modulus	C_{11}	8.567	69.72	165.7	GPa
Elastic modulus	C_{44}	1.429	26.15	79.6	GPa
Elastic modulus	C_{12}	5.710	17.43	63.9	GPa
Damping coeff.	Γ_{sl}	0.0040	0.0004	0.0004	1
Spec. impedance	Z_{sl}	3.19	12.47	19.64	MPa s m^{-1}

and experimentally [43–46]. This design is thus an obvious choice for our analysis, and following Refs. [43–46], the fluid domain Ω_{fl} in the vertical y - z plane is taken to be a rectangle of width $W_{\text{fl}} = 377 \mu\text{m}$ and height $H_{\text{fl}} = 157 \mu\text{m}$. The fluid domain is embedded in an elastic solid Ω_{sl} defined by a larger rectangle of width W_{sl} and height H_{sl} , see Fig. 2, of values to be specified below.

As sketched in Fig. 1(c), the ultrasound actuation is modeled by the time-harmonic and spatially anti-symmetric displacement condition applied to the bottom surface of the solid with a frequency in the low MHz range and a fixed amplitude $d_0 \simeq 0.1 \text{ nm}$, which corresponds to typical experimental values. This specific actuation is chosen to better generate the conventional anti-symmetric standing pressure half-wave in the horizontal direction, which focuses suspended particles in the vertical x - z plane along the center x axis of the channel. It is straightforward to extend this simple actuation model by adding an actual piezoelectric material to the solid and driving it by imposing a suitable ac voltage.

Material wise, the elastic solid in our model is taken to be the transparent thermoplastic polymethyl methacrylate (PMMA), also known as acrylic glass, Plexiglas or Lucite. The acoustofluidic response of this acoustically soft polymer is contrasted with that of the conventional acoustically hard devices made of a silicon base and a borosilicate glass lid (Pyrex) [43–46]. The values of the material parameters at ambient temperature used in the elastodynamic model of the solids are shown in Table I. Note that in the case of PMMA we have used representative average values based on Refs. [47–52]. Material parameters at 25 °C for water and 10- μm -diameter polystyrene tracer particles are listed in Table II.

III. THEORY

The physical model of the acoustophoretic device consists of a fluid-filled microchannel channel embedded in an elastic solid. The piezoelectric transducer, which in reality drives the ultrasound waves in the system, is replaced by a simplifying oscillating displacement condition on part of the outer surface of the solid. We thus need the governing equation for the linear ultrasound acoustics of

TABLE II. Material parameters at 25 °C for water and 10- μ m-diameter polystyrene tracer particles. Note: $Z_{\text{fl}} = \rho_{\text{fl}} c_{\text{fl}}$.

Parameter	Symbol	Value	Unit
<i>Water:</i>			
Mass density [40]	ρ_{fl}	997.05	kg m ⁻³
Compressibility, isentr. [40]	κ_{fl}	447.7	TPa ⁻¹
Speed of sound [40]	c_{fl}	1496.7	m s ⁻¹
Damping coefficient [55]	Γ_{fl}	0.004	1
Spec. acoustic impedance	Z_{fl}	1.49	MPa s m ⁻¹
<i>Polystyrene particles in water:</i>			
Mass density [56, 57]	ρ_{ps}	1050	kg m ⁻³
Compressibility [56, 57]	κ_{ps}	238	TPa ⁻¹
Monopole coefficient [57]	f_0	0.468	1
Dipole coefficient [57]	f_1	0.034	1

the solid and the fluid, as well as of the nonlinear acoustics describing the acoustophoretic forces on microparticles suspended in the fluid. We restrict our analysis to the time-periodic and isentropic case at ambient temperature, thus disregarding transient behavior [41] and thermal effects [40, 57].

A. Linear acoustics of the solid and the fluid

We use standard, weakly damped, linear elastodynamics [58] with the specific coupling to microscale acoustofluidics as formulated by Ley and Bruus [59] for isotropic solids, and its extension to cubic crystals by Dual and Schwarz [60]. The dynamics of the solid of density ρ_{sl} is modeled by the elastic displacement \mathbf{u} and stress $\boldsymbol{\sigma}$, both with a time-harmonic oscillation given by the phase factor $e^{-i\omega t}$, where $\omega = 2\pi f$ is the angular frequency and f is the frequency. Because the governing equations are linear, this temporal phase factor is divided out in the following, leaving only spatially dependent amplitude for all field. When time dependence is needed, the phase factor $e^{-i\omega t}$ is simply reintroduced in the fields. The linear constitutive stress-strain relation is given in terms of the elastic moduli C_{ik} in the Voigt representation, and the governing equation for the displacement field \mathbf{u} at angular frequency ω become

$$-\rho_{\text{sl}}\omega^2(1+i\Gamma_{\text{sl}})^2\mathbf{u}=\nabla\cdot\boldsymbol{\sigma},\quad\text{with}\quad(1a)$$

$$\begin{pmatrix} \sigma_{xx} \\ \sigma_{yy} \\ \sigma_{zz} \\ \sigma_{yz} \\ \sigma_{xz} \\ \sigma_{xy} \end{pmatrix} = \begin{pmatrix} C_{11} & C_{12} & C_{12} & 0 & 0 & 0 \\ C_{12} & C_{11} & C_{12} & 0 & 0 & 0 \\ C_{12} & C_{12} & C_{11} & 0 & 0 & 0 \\ 0 & 0 & 0 & C_{44} & 0 & 0 \\ 0 & 0 & 0 & 0 & C_{44} & 0 \\ 0 & 0 & 0 & 0 & 0 & C_{44} \end{pmatrix} \begin{pmatrix} \partial_x u_x \\ \partial_y u_y \\ \partial_z u_z \\ \partial_y u_z + \partial_z u_y \\ \partial_x u_z + \partial_z u_x \\ \partial_x u_y + \partial_y u_x \end{pmatrix},\quad(1b)$$

where a cubic crystal has three independent elastic moduli C_{11} , C_{12} , and C_{44} , while an isotropic material has two

due to the constraint $C_{12} = C_{11} - 2C_{44}$. In the latter case, the material is therefore characterized by the longitudinal and transverse sound speeds $c_{\text{L}} = \sqrt{C_{11}/\rho_{\text{sl}}}$ and $c_{\text{T}} = \sqrt{C_{44}/\rho_{\text{sl}}}$, respectively. The acoustic energy density $E_{\text{ac}}^{\text{sl}}$ in the solid domain is the sum of the kinetic and elastic energy densities

$$E_{\text{ac}}^{\text{sl}} = \frac{1}{2}\rho_{\text{sl}}\omega^2\langle u_k u_k \rangle + \frac{1}{2}\langle \epsilon_{ik}\sigma_{ik} \rangle,\quad(2)$$

with summation over the repeated indices $i, k = x, y, z$, and where $\epsilon_{ik} = \frac{1}{2}(\partial_i u_k + \partial_k u_i)$ is the strain tensor components, while $\langle AB \rangle = \frac{1}{2}\text{Re}[A^*B]$ is the time average over one oscillation period of the fields A and B given in the complex time-harmonic notation.

The fluid (water) of density ρ_{fl} and sound speed c_{fl} , with an acoustic pressure p and acoustic velocity \mathbf{v} at angular frequency ω , is modeled as pressure acoustics with a weak absorption $\Gamma_{\text{fl}} \ll 1$, but no viscosity, [59]

$$\nabla^2 p = -\frac{\omega^2}{c_{\text{fl}}^2}(1+i\Gamma_{\text{fl}})^2 p,\quad(3a)$$

$$\mathbf{v} = \frac{-i}{\omega\rho_{\text{fl}}}\nabla p.\quad(3b)$$

The acoustic energy density $E_{\text{ac}}^{\text{fl}}$ in the fluid domain is the sum of the kinetic and compressional energy densities,

$$E_{\text{ac}}^{\text{fl}} = \frac{1}{2}\rho_{\text{fl}}\langle v_k v_k \rangle + \frac{1}{2}\kappa_{\text{fl}}\langle p^2 \rangle,\quad(4)$$

where $\kappa_{\text{fl}} = (\rho_{\text{fl}}c_{\text{fl}}^2)^{-1}$ is the compressibility of the fluid.

B. Boundary conditions and fluid-solid coupling

The applied boundary conditions are the usual ones [59], namely that (1) the stress and the velocity fields are continuous across all fluid-solid interfaces, which then provides the coupling between the fluid and solid domains, (2) the stress is zero on all outer boundaries facing the air, and (3) the piezoelectric actuation is represented by a given displacement in the normal direction at that part of the solid surface, where the actuator is attached. The influence (\leftarrow) from the surroundings on a given domain with an outward-pointing surface normal \mathbf{n} is

$$\text{Fluid domain } \leftarrow \text{ solid:} \quad \mathbf{v} \cdot \mathbf{n} = -i\omega \mathbf{u} \cdot \mathbf{n} \quad (5a)$$

$$\text{Solid domain } \leftarrow \text{ fluid:} \quad \boldsymbol{\sigma}_{\text{sl}} \cdot \mathbf{n} = -p\mathbf{n}, \quad (5b)$$

$$\text{Solid domain } \leftarrow \text{ transducer:} \quad \mathbf{u} = \pm d_0 \mathbf{n}, \quad (5c)$$

$$\text{Solid domain } \leftarrow \text{ air:} \quad \boldsymbol{\sigma}_{\text{sl}} \cdot \mathbf{n} = \mathbf{0}, \quad (5d)$$

C. The acoustic radiation force on suspended microparticles

In a good acoustofluidic device, the acoustic radiation force \mathbf{F}^{rad} on a suspended microparticle should be sufficiently large. In this work we consider 10- μ m-diameter

spherical polystyrene "Styron 666" (ps) particles with density ρ_{ps} and compressibility κ_{ps} . For such a large microparticle suspended in water of density ρ_{fl} and compressibility κ_{fl} , thermoviscous boundary layers can be neglected, and the monopole and dipole acoustic scattering coefficients f_0 and f_1 are given by [57],

$$f_0 = 1 - \frac{\kappa_{\text{ps}}}{\kappa_{\text{fl}}} = 0.468, \quad f_1 = \frac{2(\rho_{\text{ps}} - \rho_{\text{fl}})}{2\rho_{\text{ps}} + \rho_{\text{fl}}} = 0.034. \quad (6)$$

In the presence of an acoustic field (3) of pressure p and velocity \mathbf{v} , the suspended microparticle experience an acoustic radiation force \mathbf{F}^{rad} given by [61]

$$\mathbf{F}^{\text{rad}} = -\pi a^3 \left(\frac{2}{3} \kappa_{\text{fl}} \text{Re}[f_0^* p^* \nabla p] - \rho_{\text{fl}} \text{Re}[f_1^* \mathbf{v}^* \cdot \nabla \mathbf{v}] \right). \quad (7)$$

Here, a is the particle radius, and the asterisk denotes complex conjugation.

D. Numerical implementation

Following the procedure described in Ref. [59], including mesh convergence tests, the coupled field equations (1) and (3) for the fluid pressure p and the elastic-solid displacement \mathbf{u} , subject to the boundary conditions Eq. (5), are implemented and solved on weak form using the finite-element solver Comsol Multiphysics 5.3a [62]. Lastly, to evaluate the quality of the acoustophoresis in the given device, the last step is to use Eqs. (6) and (7) to compute the acoustic scattering coefficients f_0 and f_1 as well as the acoustic radiation force \mathbf{F}^{rad} acting on a single 10- μm -diameter spherical polystyrene tracer bead suspended at different positions in the water-filled microchannel.

IV. RESULTS FOR THE 2D MODEL OF A CONVENTIONAL HARD-WALLED DEVICE

We begin our analysis with the computational less demanding and faster simulations restricted to 2D cross sections of the systems, before moving on to the more heavy, full 3D simulations. Moreover, to establish a baseline for evaluating the results for the acoustophoretic capabilities of all-polymer devices, we first analyze an ideal hard-walled device. Then we progress to a conventional, acoustically hard, but elastic silicon-glass device, before finally treating an all-polymer device.

A. An ideal hard-walled device in 2D

We consider a rectangular channel cross section of width W_{fl} and height H_{fl} in the vertical y - z plane and centered around $y = 0$. If its walls are infinitely hard, it

TABLE III. The length scales of the rectangular silicon-Pyrex (si-py) system with a fluid-filled rectangular channel (fl). The values are from Ref. [43], except ΔW introduced in Fig. 2(b).

Dimension	Solid domain	Fluid domain
Length	$L_{\text{sl}} = 50 \text{ mm}$	$L_{\text{fl}} = 40 \text{ mm}$
Width	$W_{\text{sl}} = 2.52 \text{ mm}$	$W_{\text{fl}} = 377 \text{ }\mu\text{m}$
Height	$H_{\text{sl}} = 350 \text{ }\mu\text{m}$	$H_{\text{fl}} = 157 \text{ }\mu\text{m}$
Height	$H_{\text{py}} = 1130 \text{ }\mu\text{m}$	—
Actuator gap	$\Delta W = 100 \text{ }\mu\text{m}$	—

supports a standing half-wave pressure resonance p_{hard} in the horizontal y -direction at the frequency f_{hard} . The resonance is characterized by its amplitude p_{ac} and corresponding acoustic energy density E_{hard} , and it results in a radiation force $\mathbf{F}_{\text{hard}}^{\text{rad}}$ of amplitude $F_{\text{ac}}^{\text{rad}}$ on a given spherical tracer particle of radius a and acoustic monopole and dipole scattering coefficients f_0 and f_1 suspended in the channel. Using the dimensions of the fluid domain listed in Table III, the resonance properties can be summarized as, [45]

$$f_{\text{hard}} = \frac{c_{\text{fl}}}{2W_{\text{fl}}} = 1.985 \text{ MHz}, \quad (8a)$$

$$p_{\text{hard}} = p_{\text{ac}} \sin(k_y y), \quad \text{with } k_y = \frac{\pi}{W_{\text{fl}}}, \quad (8b)$$

$$E_{\text{hard}} = \frac{1}{4} \kappa_{\text{fl}} p_{\text{ac}}^2, \quad (8c)$$

$$\mathbf{F}_{\text{hard}}^{\text{rad}} = -F_{\text{ac}}^{\text{rad}} \sin(2k_y y) \mathbf{e}_y, \quad (8d)$$

$$\text{with } F_{\text{ac}}^{\text{rad}} = \left[\frac{f_0}{3} + \frac{f_1}{2} \right] 4\pi^2 \frac{a^3 E_{\text{hard}}}{W_{\text{fl}}}.$$

This hard-walled resonance is completely decoupled from the motion of the surrounding solid. Its standing pressure wave p_{hard} is a perfect sinusoidal half-wave with a vertical nodal line at the channel center, and the radiation force $\mathbf{F}_{\text{hard}}^{\text{rad}}$ is similarly a perfect sinusoidal full-wave that pushes suspending particles horizontally towards their stable equilibrium positions at the vertical center plane of the channel. No vertical force is exerted.

The f_{hard} resonance is an idealization of the standing pressure half wave used in many acoustophoresis experiments. In the following study, we choose this resonance as the prime example of an acoustic resonance that leads to particularly good acoustophoresis.

B. A conventional silicon-glass device in 2D

As mentioned in the introduction, silicon-glass devices have successfully been applied to microscale acoustofluidic tasks [6–9, 12, 13]. Following the experiments of Refs. [43–46], we choose here to study the long, straight rectangular channel of length L_{fl} , width W_{fl} , and height H_{fl} fabricated by KOH etch into the surface of a rectangular $\langle 100 \rangle$ silicon (Si) wafer with length L_{sl} , width W_{sl} ,

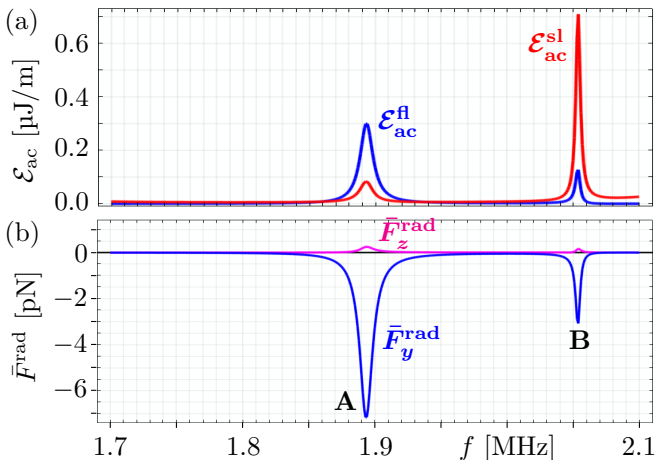


FIG. 3. Numerical results for the frequency dependency of the rectangular silicon-glass device actuated at frequency f using the anti-symmetric actuation of Fig. 2(b) with displacement amplitude $d_0 = 0.1$ nm. Two strong resonances A and B are identified. (a) Line plot of the total acoustic energy \mathcal{E}_{ac}^{fl} (blue) in the fluid domain Ω_{fl} and \mathcal{E}_{ac}^{sl} (red) in the solid domain Ω_{sl} versus f for the silicon-glass device. (b) The spatially averaged radiation force components \bar{F}_y^{rad} (blue) and \bar{F}_z^{rad} (magenta).

and height $H_{si} = H_{sl}^{bot} + H_{fl}$, which is sealed off with a borosilicate glass lid (Pyrex) of height $H_{py} = H_{sl}^{top}$ and the same length L_{sl} and width W_{sl} . In the following, we restrict our modeling to the 2D vertical cross section in the y - z plane sketched in Fig. 2(a) using the device dimensions listed in Table III and the anti-symmetric actuation of amplitude $d_0 = 0.1$ nm on the bottom surface as sketched in Fig. 2(b) and given in Eq. (5c).

Most of the theoretical analysis of the acoustofluidic properties of this microchannel has been carried out using the assumption of infinitely hard walls [39–41]. This assumption is justified for silicon-glass devices, as these solids are heavier and stiffer than water, as quantified by the ratio Z_{sl}/Z_{fl} of the specific acoustic impedances listed in Tables I and II,

$$\frac{Z_{sl}^{py}}{Z_{fl}^{wa}} = 8.35, \quad \frac{Z_{sl}^{si}}{Z_{fl}^{wa}} = 13.16. \quad (9)$$

However, as in Ref. [42], we now include the elastic properties of the surrounding elastic silicon and Pyrex material using the parameter values listed in Table I.

According to Eq. (8a), the hard-walled device has a well-defined half-wave resonance at $f_{hard} = 1.985$ MHz. We therefore simulate the silicon-glass device in the frequency range from 1.7 to 2.1 MHz, see Fig. 3. We compute the frequency dependency of the acoustic energy \mathcal{E}_{ac}^{sl} and \mathcal{E}_{ac}^{fl} in the solid and fluid domain, defined by

$$\mathcal{E}_{ac}^{sl} = \int_{\Omega_{sl}} E_{ac}^{sl} dydz, \quad \mathcal{E}_{ac}^{fl} = \int_{\Omega_{fl}} E_{ac}^{fl} dydz. \quad (10)$$

TABLE IV. The fluid-domain-averaged acoustic energy density E_{ac}^{fl} , the components of the average acoustic radiation force \bar{F}^{rad} and the figure of merit R for the resonances A and B of Fig. 3 in the silicon-glass device of width $W_{sl} = 2.52$ mm and height $H_{sl} = 1.48$ mm, and $d_0 = 0.1$ nm.

Resonance number	Frequency [MHz]	E_{ac}^{fl} [Pa]	\bar{F}_y^{rad} [pN]	\bar{F}_z^{rad} [pN]	R [1]
A	1.893	5.07	7.15	0.25	29.1
B	2.054	2.15	3.08	0.17	18.1

as well as of the spatial average \bar{F}^{rad} of the acoustic radiation force on a 10- μ m-diameter test particle in the fluid domain,

$$\bar{F}_y^{rad} = \frac{1}{W_{fl}H_{fl}} \int_{\Omega_{fl}} \frac{y}{|y|} F_y^{rad} dydz, \quad (11a)$$

$$\bar{F}_z^{rad} = \frac{1}{W_{fl}H_{fl}} \int_{\Omega_{fl}} |F_z^{rad}| dydz. \quad (11b)$$

Here, we have "rectified" the y -component average through the anti-symmetric pre-factor $y/|y|$ to obtain a large value of \bar{F}_y^{rad} , when F_y^{rad} has the useful anti-symmetric form, and where we have taken the absolute value of F_z^{rad} before averaging, so that a minimal value of \bar{F}_z^{rad} is obtained, when the magnitude of the vertical component of the acoustic radiation force is small everywhere. This is done to help identifying resonances having a behavior similar to the conventional and very useful one of the hard-walled device, see Eq. (8).

The results for \mathcal{E}_{ac}^{sl} , \mathcal{E}_{ac}^{fl} , \bar{F}_y^{rad} , and \bar{F}_z^{rad} versus frequency are shown in Fig. 3. We readily identify two strong resonances A and B that show up in all four quantities at $f_A = 1.893$ MHz and $f_B = 2.054$ MHz, respectively. Acoustically, these resonances are different. In Fig. 3(a) we see that for resonance A, the acoustic energy $\mathcal{E}_{ac}^{fl} = 0.300$ J/m in the fluid is 3.7 times larger than $\mathcal{E}_{ac}^{sl} = 0.082$ J/m in the solid, in spite of the area $\mathcal{A}_{fl} = 0.059$ mm² of the fluid domain is 62 times smaller than the area $\mathcal{A}_{sl} = 3.670$ mm² of the solid domain. Thus, A may be characterized as a fluid-domain resonance. Conversely, for resonance B, $\mathcal{E}_{ac}^{fl} = 0.127$ J/m in the fluid is 0.18 times $\mathcal{E}_{ac}^{sl} = 0.710$ J/m in the solid, and B may thus be characterized as a whole-system resonance. In Fig. 3(b) we observe that for both resonance A and B, the magnitude \bar{F}_y^{rad} of the horizontal component of \bar{F}^{rad} is much larger than that of the vertical component \bar{F}_z^{rad} . To quantify this, we introduce the figure of merit R , listed in Table IV, as the ratio

$$R = -\frac{\bar{F}_y^{rad}}{\bar{F}_z^{rad}}. \quad (12)$$

R will be large in situations, where the acoustic radiation force has the desired property of a large anti-symmetric

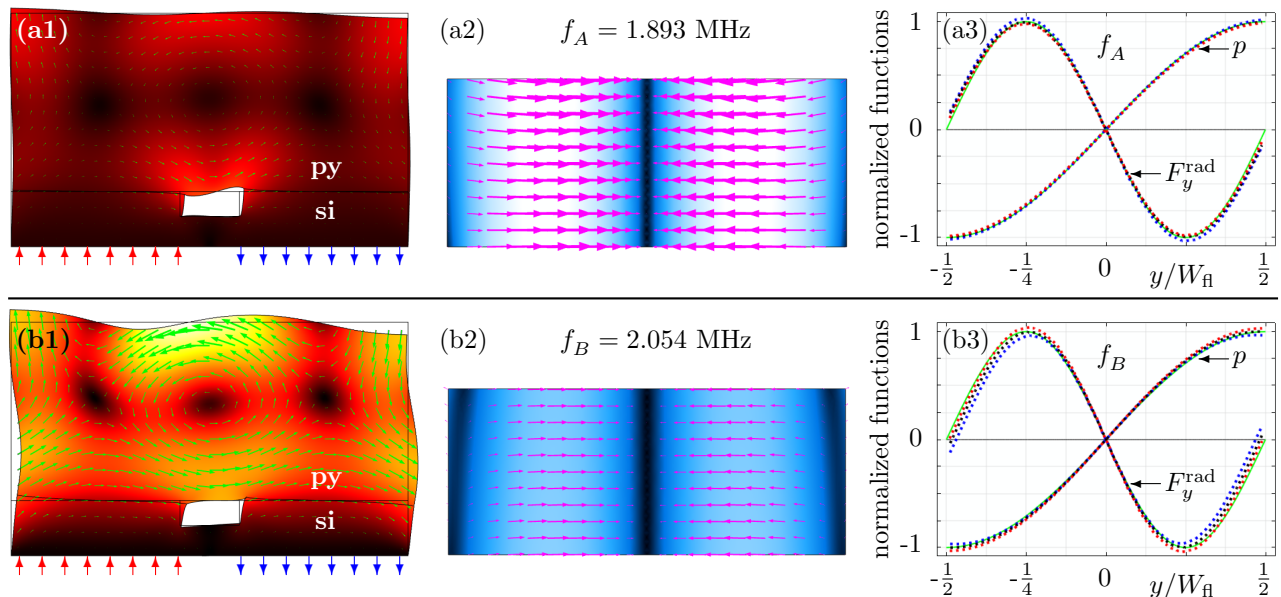


FIG. 4. Numerical results for resonance A and B in Fig. 3 of the glass-silicon device. Top row (a1), (a2), and (a3) are for $f_A = 1.893$ MHz. (a1) Vector plot in the solid domain Ω_{sl} of the displacement field \mathbf{u} (green arrows) and color plot of its amplitude u from 0 nm (black) to 2.6 nm (white). To be visible, the nm-scale displacement has been increased by a factor 50,000. (a2) The radiation force \mathbf{F}^{rad} on a 10- μm -diameter spherical polystyrene tracer particle as a function of its position in the fluid domain Ω_{fl} . Color plot of the magnitude F^{rad} from 0 pN (black) to 11.5 pN (white) and vector plot (magenta arrows) of \mathbf{F}^{rad} . (a3) Comparison of the numerical simulation of the silicon-glass device (dotted lines) of Fig. 3 with the analytical result of the hard-wall device (solid green line). The normalized pressure p/p_{norm} (half wave, $p_{\text{norm}} = 209$ kPa) and the y -component $F_y^{\text{rad}}/F_{\text{norm}}^{\text{rad}}$ of the radiation force (full wave, $F_{\text{norm}}^{\text{rad}} = 11.0$ pN) plotted along the top, center, and bottom horizontal lines at $z = 0.9H_{\text{fl}}$ (blue dots), $z = 0.5H_{\text{fl}}$ (black dots), and $z = 0.1H_{\text{fl}}$ (red dots), respectively. Bottom row (b1), (b2), and (b3) are as top row (a1), (a2), and (a3), respectively, but for $f_B = 2.054$ MHz with $p_{\text{norm}} = 138$ kPa and $F_{\text{norm}}^{\text{rad}} = 5.05$ pN.

horizontal component and small vertical component. For the two resonances the figure of merit is $R_A = 29.1$ and $R_B = 18.1$, respectively, indicating that the fluid-domain resonance A has better acoustophoretic properties than the whole-system resonance B. We also note that the predicted acoustic energy density E_{ac} at the two resonances listed in Table IV, resulting from the chosen actuation amplitude $d_0 = 0.1$ nm, are in agreement with typical experimental values that fall in the range from 1 to 100 Pa [43–46].

We study resonance A and B in more detail in Fig. 4. The color and vector plots in Figs. 4(a1) and 4(b1) reveal that of the displacement \mathbf{u} for resonance A is much larger at the interface to the channel than at the outer surface, while for resonance B the opposite is true. The color and vector plot of the acoustic radiation force \mathbf{F}^{rad} for resonance A in Fig. 4(a2), shows that it is nearly identical to the perfectly horizontal radiation force $\mathbf{F}_{\text{hard}}^{\text{rad}}$ in Eq. (8d) of the hard-walled device with its vertical line of stability in the center of the channel. As seen in Fig. 4(b2), resonance B is weaker, but is quite similar except for some skewness at the sides. Finally, through the horizontal line plots of the radiation force F_y^{rad} and the pressure p at the top, center, and bottom heights $z = 0.9H_{\text{fl}}$, $0.5H_{\text{fl}}$, and $0.1H_{\text{fl}}$ shown in Figs. 4(a3) and 4(b3), we

compare more closely resonance f_A and f_B in the silicon-glass device with the ideal half-wave resonance f_{hard} in the hard-walled device. It is seen how closely the pressure p and the y -component F_y^{rad} of the radiation force at the resonance f_A reproduce the corresponding analytical expressions Eqs. (8b) and (8d) of the resonance f_{hard} . Resonance f_B deviates a little more from resonance f_{hard} .

In conclusion, Figs. 3 and 4 demonstrate that in an acoustically hard silicon-glass device, two types of resonances may exist. One type is the fluid-domain resonance, represented by resonance A, defined by a high acoustic energy in the fluid domain and relatively little coupling to the solid domain. Compared to the actuation displacement d_0 , the amplitude u of displacement field is relatively large at the inner fluid-solid interface and small at the outer surface of the solid. The resulting acoustic fields and radiation force closely resemble those of the ideal hard-walled case. Conversely, the other type is the whole-system resonance, represented by resonance B, defined by a high acoustic energy in the solid domain and a low one in the fluid domain. The displacement at the outer surface of the solid is larger than at the inner fluid-solid interface. The resulting acoustic fields and radiation force deviate a little from those of the ideal hard-walled case.

V. RESULTS FOR THE 2D MODEL OF AN ALL-POLYMER PMMA DEVICE

We now apply our model to the study of an acoustically soft PMMA device. We do expect to see a different behavior compared to the acoustically hard silicon-glass device, because of the small ratio $Z_{\text{sl}}/Z_{\text{fl}}$ of the specific acoustic impedances listed in Tables I and II,

$$\frac{Z_{\text{sl}}^{\text{PMMA}}}{Z_{\text{fl}}^{\text{wa}}} = 2.14, \quad (13)$$

which is 4 to 7 times smaller than those of pyrex and silicon given in Eq. (9). In particular, we expect the fluid-domain resonances of type A to vanish in this case, leaving only whole-system ultrasound resonances (WSUR) of type B.

A. Analysis of the 3-mm wide PMMA device

To investigate this hypothesis, we perform numerical simulations on a PMMA device with the dimensions listed in Table V. These values refer to the preliminary experimental work carried out by Pelle Ohlsson and Ola Jakobsson at the company AcouSort AB in Lund, Sweden, on acoustophoresis in all-polymer devices [63]. The device is fabricated from a thin bottom-layer PMMA film of height $H_{\text{sl}}^{\text{bot}}$ and width W_{sl} , see Fig. 2(a), onto which is bonded a thick PMMA block of height $H_{\text{sl}}^{\text{top}} + H_{\text{fl}}$ and same width W_{sl} that contains a rectangular channel of height H_{fl} and width W_{fl} embossed or milled into its bottom surface. In the model we again use the anti-symmetric actuation of Fig. 2(b), typically in the range from 1 to 2.1 MHz, but now with the larger actuation displacement amplitude $d_0 = 0.3$ nm to mimic the softer material.

The results for $\mathcal{E}_{\text{ac}}^{\text{sl}}$, $\mathcal{E}_{\text{ac}}^{\text{fl}}$, \bar{F}_y^{rad} , and \bar{F}_z^{rad} versus frequency in the PMMA device are shown in Fig. 5. Right away, we notice one striking difference between these spectra and the one for the silicon-glass device in Fig. 3. All the observed resonances are whole-system resonances of type B. The energy $\mathcal{E}_{\text{ac}}^{\text{sl}}$ of the solid is one to two orders of magnitude larger than the energy $\mathcal{E}_{\text{ac}}^{\text{fl}}$ of the fluid domain. In fact, in Fig. 5(a) we need to use a logarithmic scale to be able to see these two energies in the same

TABLE V. The length scales of the rectangular PMMA system (sl) with a fluid-filled rectangular channel (fl). The values are provided by AcouSort [63].

Dimension	Solid domain	Fluid domain
Length	$L_{\text{sl}} = 50$ mm	$L_{\text{fl}} = 40$ mm
Width	$W_{\text{sl}} = 3.0$ mm	$W_{\text{fl}} = 375$ μm
Height	$H_{\text{sl}}^{\text{bot}} = 175$ μm	$H_{\text{fl}} = 150$ μm
Height	$H_{\text{sl}}^{\text{top}} + H_{\text{fl}} = 1000$ μm	—
Actuator gap	$\Delta W = 100$ μm	—

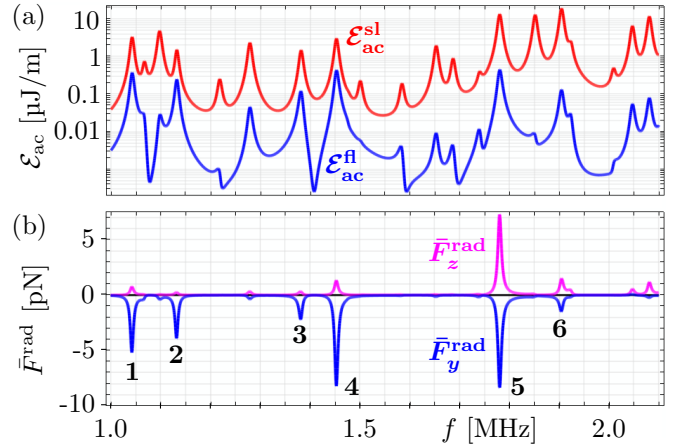


FIG. 5. Numerical results for the rectangular PMMA device actuated at frequency f using the anti-symmetric actuation of Fig. 2(b) with displacement amplitude $d_0 = 0.3$ nm. (a) Log-lin plot of the total acoustic energy $\mathcal{E}_{\text{ac}}^{\text{fl}}$ (blue) in the fluid domain Ω_{fl} and $\mathcal{E}_{\text{ac}}^{\text{sl}}$ (red) in the solid domain Ω_{sl} versus actuation frequency f . (b) The spatially averaged radiation force components \bar{F}_y^{rad} (blue line) and \bar{F}_z^{rad} (magenta line) as a function of the actuation frequency f showing six prominent resonances 1–6.

plot. In Fig. 5(b) we plot the average acoustic radiation force components \bar{F}_y^{rad} and \bar{F}_z^{rad} , and as before observe that a number of resonances are clearly identified in all four quantities.

The six most prominent resonances and their figure of merit R are listed in Table VI. Based on these data, we predict that resonance 2 at $f_2 = 1.1320$ MHz with the highest figure of merit, $R_2 = 14.9$, has properties resembling those of the ideal resonance f_{hard} the most, while resonance 6 at $f_6 = 1.9045$ MHz, the one closest to the ideal resonance frequency $f_{\text{hard}} = 2.0$ MHz, is not good given its low figure of merits $R_6 = 1.0$.

This hypothesis is checked in Fig. 6. We see that indeed most of the physical properties of PMMA resonance 2 in Fig. 6(a1), (a2), and (a3) are similar to the almost perfect silicon-glass resonance f_A . In one aspect

TABLE VI. The fluid-domain-averaged acoustic energy density $E_{\text{ac}}^{\text{fl}}$, the components of the average acoustic radiation force $\bar{\mathbf{F}}^{\text{rad}}$ and the figure of merit R for each of the six pronounced resonances of Fig. 5 in the 2D PMMA device of width $W_{\text{sl}} = 3$ mm and height $H_{\text{sl}} = 1.175$ mm, and $d_0 = 0.3$ nm.

Resonance number	Frequency [MHz]	$E_{\text{ac}}^{\text{fl}}$ [Pa]	\bar{F}_y^{rad} [pN]	\bar{F}_z^{rad} [pN]	R [1]
1	1.0425	6.63	5.19	0.78	6.7
2	1.1320	4.40	3.91	0.26	14.9
3	1.3815	2.14	2.21	0.34	6.6
4	1.4530	7.72	8.22	1.34	6.1
5	1.7810	7.93	8.36	7.27	1.2
6	1.9045	2.32	1.50	1.48	1.0

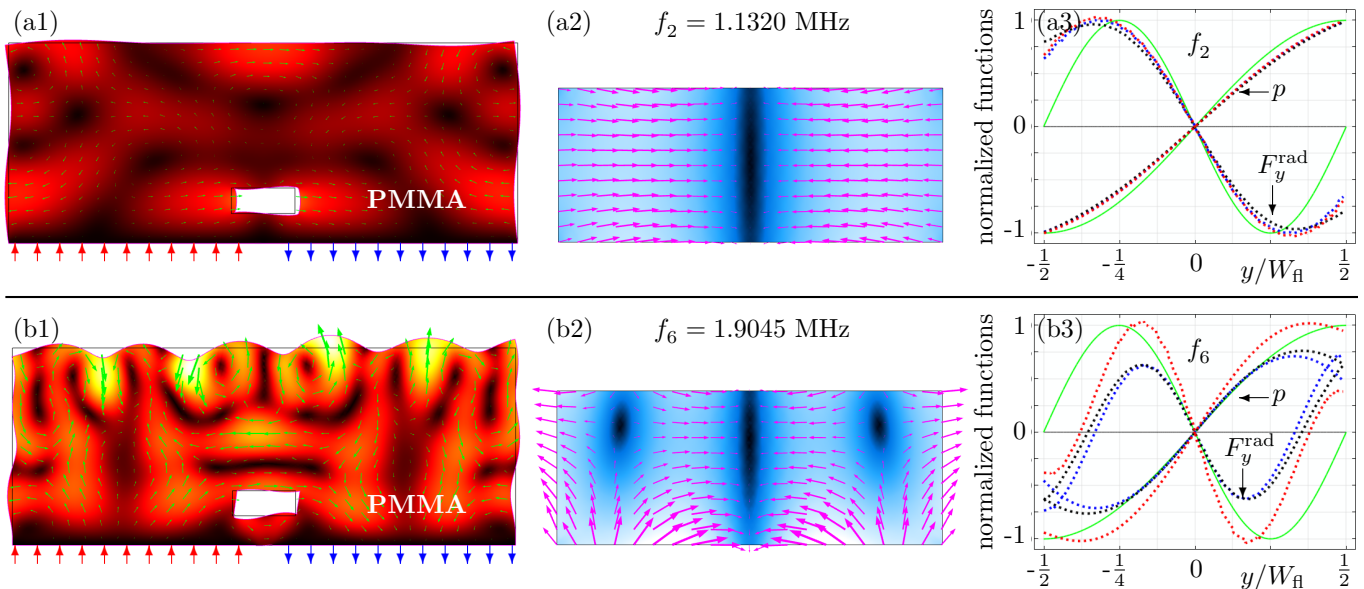


FIG. 6. Numerical results for resonance 2 and 6 in Fig. 5 of the PMMA device. Top row (a1), (a2), and (a3) are for $f_2 = 1.1320$ MHz. (a1) Vector plot in the solid domain Ω_{sl} of the displacement field \mathbf{u} (green arrows) and color plot of its amplitude u from 0 nm (black) to 25 nm (light yellow). To be visible, the nm-scale displacement has been increased by a factor 3000. (a2) The radiation force \mathbf{F}^{rad} on a 10- μm -diameter spherical polystyrene tracer particle as a function of its position in the fluid domain Ω_{fl} . Color plot of the magnitude F^{rad} from 0 pN (black) to 9 pN (white) and vector plot (magenta arrows) of \mathbf{F}^{rad} . (a3) The normalized pressure p/p_{norm} (half wave, $p_{\text{norm}} = 150$ kPa) and the y -component $F_y^{\text{rad}}/F_{\text{norm}}^{\text{rad}}$ of the radiation force (full wave, $F_{\text{norm}}^{\text{rad}} = 5.4$ pN) along the top, center, and bottom horizontal lines at $z = 0.9H_{fl}$ (blue dots), $z = 0.5H_{fl}$ (black dots), and $z = 0.1H_{fl}$ (red dots), respectively. Bottom row (b1), (b2), and (b3) are as top row (a1), (a2), and (a3), respectively, but for $f_6 = 1.9045$ MHz with $p_{\text{norm}} = 135$ kPa and $F_{\text{norm}}^{\text{rad}} = 6.8$ pN.

it is even superior: The radiation force in resonance f_2 is not zero at the channel walls $y = \pm \frac{1}{2}W_{fl}$ as is the case with f_A and f_{hard} . In this sense f_2 is better to move particles from any starting point in the channel towards the vertical nodal line at $y = 0$. In contrast, the plots in Fig. 6(b1), (b2), and (b3) show that the acoustics in the channel, induced by the whole-system resonance in the PMMA device, results in a radiation force that only in the middle part of the fluid domain points towards the center line. At the edges it points the opposite way. Also a strong vertical component is observed. Clearly in this case, the low figure of merit is correctly predicting a resonance not well suited for acoustophoretic applications corresponding to the acoustically hard system.

With this example, we have demonstrated the main point of the paper: Microchannels embedded in acoustically sort materials are not able to support a resonance close to the ideal hard-wall resonance. However, whole-system resonances, primarily defined by having a relatively big displacement field in the large solid domain, may nevertheless induce a pressure field in the small fluid domain, which have properties suitable for acoustophoretic applications. We have identified these few acoustophoretically useful whole-system resonances as those peaks in the spectra of the energy and the radiation force components that have the largest figure of merit R .

B. The width dependence of the PMMA device

We further demonstrate the use the above whole-system-ultrasound-resonance principle, by studying the width dependency of the resonances in the PMMA device. In Fig. 7 we show a scatter plot of resonances as a function of the device width W_{sl} from 1 to 6 mm and of the actuation frequency f_0 from 1 to 2.1 MHz. The area of each data point is proportional to the magnitude \bar{F}_y^{rad} . The maximal amplitude is $\bar{F}_y^{\text{rad}} = 337$ pN obtained for $W_{sl} = 1.3$ mm and $f = 1.328$ MHz, and we have left out resonances with a magnitude lower than $\bar{F}_y^{\text{rad}} = 0.3$ pN. The color code of the points goes from black at $\bar{F}^{\text{rad}} = 0.03$ pN to yellow at $\bar{F}^{\text{rad}} = 30$ pN.

To visualize the figure of merit R of the resonance points in Fig. 7, we have added a thick black rim to the resonance points with $R \geq 10$ and a thin black rim to points with $5 \leq R < 10$. The highest figure of merit is $R = 27.3$ obtained for $W_{sl} = 3.5$ mm and $f = 1.054$ MHz. Using such a plot, we are able to efficiently map out the parameter space in the hunt for suitable device designs for making all-polymer devices able to produce good acoustophoresis.

It is clear from Fig. 7 that the acoustophoretically good resonance 2 lies on a curve of resonance points for which the resonance frequency increases as the device width W_{sl}

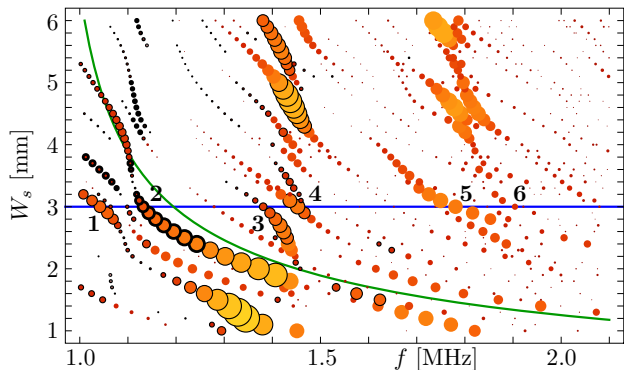


FIG. 7. The average radiation force component \bar{F}_y^{rad} in the fluid domain in a PMMA device at resonance for a 10- μm -diameter polystyrene tracer particle plotted as a colored scatter plot from 0.03 pN (black) to 30 pN (yellow) versus the polymer chip width W_{sl} and the actuation frequency f . The area of each data point is proportional to the magnitude of \bar{F}_y^{rad} . Resonances with a figure of merit $5 \leq R < 10$ and $10 \leq R$ are further marked with a thin black and thick black rim, respectively. The horizontal blue line and the resonances 1, 2, ..., 6 correspond to the line plot in Fig. 5. The green curve is the simplified analytical prediction $W_{\text{sl}}^{(\frac{1}{2},1)}$, Eq. (14).

decreases. To understand this behavior, we study more closely the displacement field of resonance 2 in Fig. 6(a). We note that not only is there half a shear wave along the y axis due to the actuation, but there is also a full shear wave along the z axis. This resonance we denote the $(\frac{1}{2},1)$ -resonance. In a simplistic model of shear-wave

propagation of velocity c_T decoupled from the longitudinal wave, we predict the resonance frequency $f_{(\frac{1}{2},1)}$ for the $(\frac{1}{2},1)$ -resonance to be

$$f_{(\frac{1}{2},1)} = c_T \sqrt{\frac{2^2}{W_{\text{sl}}^2} + \frac{1^2}{H_{\text{sl}}^2}} \quad \text{or} \quad W_{\text{sl}}^{(\frac{1}{2},1)}(f) = \frac{2}{\sqrt{\frac{f^2}{c_T^2} - \frac{1}{H_{\text{sl}}^2}}}. \quad (14)$$

As seen from Fig. 7 (green curve), this naive prediction is in fair agreement with the line of resonant points to which resonance 2 belongs. At the position of the fluid domain, this particular shear wave results in a horizontal oscillating displacement field which is compatible with ideal standing pressure half-wave in the channel.

VI. RESULTS FOR THE 3D MODEL OF AN ALL-POLYMER PMMA DEVICE

A more realistic test of the whole-system-resonance principle for a device in 3D is shown in Fig. 8 for a microchannel of length $L_{\text{fl}} = 40$ mm embedded in PMMA chip of length $L_{\text{sl}} = 50$ mm and with the same 2D cross section as above, see Table V. The ultrasound actuation of amplitude $d_0 = 0.3$ nm is anti-symmetric in the y direction and independent of x along the entire bottom as sketched Fig. 2(b). The whole-system-resonance principle is now used to identify resonances useful for acoustophoresis in this coupled polymer-water systems.

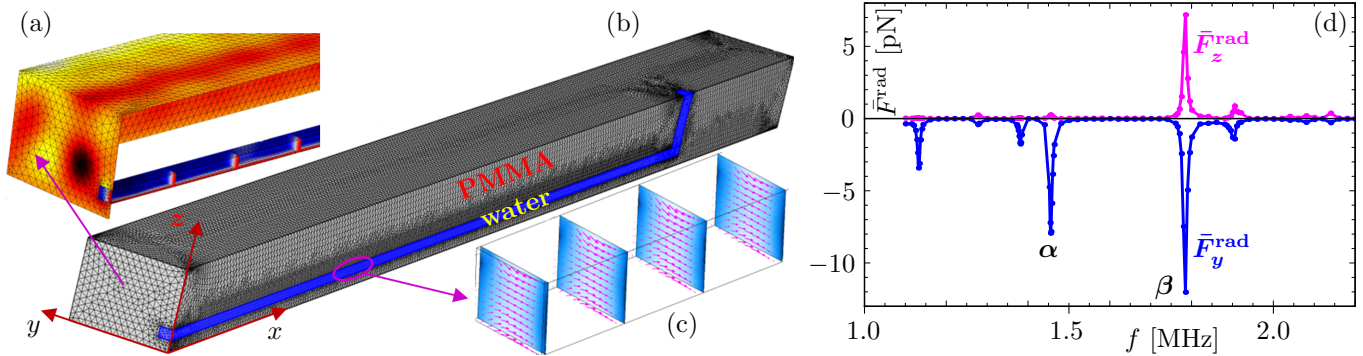


FIG. 8. Numerical simulation of a water-filled microchannel of length $L_{\text{fl}} = 40$ mm, width $W_{\text{fl}} = 375$ μm , and height $H_{\text{fl}} = 150$ μm embedded in a PMMA chip of length $L_{\text{sl}} = 50$ mm, width $W_{\text{sl}} = 3$ mm, and height $H_{\text{sl}} = 1175$ μm , and actuated at the resonance frequency $f = 1.455$ MHz. Due to the symmetry at the yz - and xz -plane, only the quarter domain $0 < x < \frac{1}{2}L_{\text{sl}}$ and $0 < y < \frac{1}{2}W_{\text{sl}}$ is simulated as in Ref. [59]. The anti-symmetric actuation of Fig. 2(b) is used with amplitude $d_0 = 0.3$ nm. (a) Color plots of the amplitude of the displacement u from 0 nm (black) to 4.5 nm (white) on the outer PMMA surface and the pressure p from 0 kPa (red) to 190 kPa (blue) near the symmetry plane $x = 0$ of the system. (b) The finite-element mesh (thin gray lines) used in the simulation. (c) The radiation force \mathbf{F}^{rad} on 10- μm -diameter polystyrene tracer particles in a short section of the microchannel. (d) The frequency dependency of the volume-averaged acoustic radiation force components \bar{F}_y^{rad} and \bar{F}_z^{rad} showing two pronounced resonances α and β at $f_{\alpha} = 1.455$ MHz and $f_{\beta} = 1.785$ MHz.

TABLE VII. The fluid-domain-averaged acoustic energy density E_{ac}^{fl} , the components of the average acoustic radiation force $\bar{\mathbf{F}}^{rad}$ and the figure of merit R for resonances α and β Fig. 8(d) in the 3D PMMA device of length $L_{sl} = 50$ mm, width $W_{sl} = 3$ mm and height $H_{sl} = 1.175$ mm, and anti-symmetric actuation of amplitude $d_0 = 0.3$ nm.

Resonance number	Frequency [MHz]	E_{ac}^{fl} [Pa]	\bar{F}_y^{rad} [pN]	\bar{F}_z^{rad} [pN]	R [1]
α	1.455	4.00	7.94	0.24	32.5
β	1.785	3.63	12.06	7.18	1.7

The frequency dependent volume-averaged acoustic radiation force \bar{F}_y^{rad} is shown in Fig. 8(d), and it reveals two strong resonances α and β at $f_\alpha = 1.455$ MHz and at $f_\beta = 1.785$ MHz with properties listed in Table VII. Their respective figures of merit $R_\alpha = 32.5$ and $R_\beta = 1.7$ indicate that resonance α is more likely to have good properties for acoustophoresis. This is verified by the detailed structure of the pressure field in Fig. 8(a) and the acoustic radiation force \mathbf{F}^{rad} represented by four vertical cut-planes in Fig. 8(c). The acoustic energy density at resonance α is predicted to be $E_{ac}^{fl} = 4.0$ Pa for the assumed actuation amplitude $d_0 = 0.3$ nm.

Preliminary experiments performed by Pelle Ohlson and Ola Jakobsson at AcouSort AB in Lund, Sweden, on PMMA devices nominally identical to the one simulated here, have confirmed the existence of a whole-system ultrasound resonance at $f = 1.55$ MHz with an acoustic energy density of $E_{ac}^{fl} = 12$ Pa, fully capable of obtaining acoustophoretic focusing on suspended 10- μ m-diameter polystyrene tracer particles [63]. The predicted whole-system resonance frequency $f_\alpha = 1.455$ MHz is only 6 % lower than the observed one, but 27 % lower than the hard-wall resonance, and the predicted acoustic energy density $E_{ac} = 4$ Pa will equal the observed one, if the assumed actuation amplitude is increased by a factor of $\sqrt{12 \text{ Pa}/4 \text{ Pa}} = 1.7$ from $d_0 = 0.3$ nm to $d_0 = 0.5$ nm. A detailed report of these experiments and their comparison with simulations will be given elsewhere.

VII. CONCLUDING DISCUSSION

We have presented a numerical study of an acoustically soft device consisting of a fluid channel inside a PMMA chip, where a single split or two separate ultrasound transducers operate in anti-phase to excite a standing ultrasound wave in the entire polymer chip. The model takes into account the fully coupled longitudinal and transverse displacement waves in the solid domain and their coupling with the pressure field in the fluid

domain.

The nearly identical specific acoustic impedances for PMMA (and other polymers) and water does not allow for localized resonances in the water domain that are decoupled from the solid domain, as is usually the case in acoustically hard systems such as the conventional silicon-glass devices. Thus for all-polymer systems, the conventional thinking in terms of standing half-wave resonances in the fluid domain cannot be maintained. Instead, the acoustic fields in the two domains are strongly coupled, and given its large volume compared to the fluid domain, the resonance behavior is mainly determined by the solid domain.

Nevertheless, we have found whole-system ultrasound resonances (WSUR) that supports good acoustophoretic action in the water channel. These WSUR resonances can be identified theoretically by computing resonance peaks in the area-averaged (in 2D) or volume-averaged (in 3D) acoustophoretic force component \bar{F}_y^{rad} by Eq. (11) in combination with the figure of merit R defined in Eq. (12). We have demonstrated in both 2D and 3D models, how such WSUR resonance indeed have acoustic properties that are comparable to those found in conventional systems used for acoustophoresis.

Preliminary experiments performed at AcouSort AB [63] on the specific PMMA system modeled here in 3D, have verified the existence of WSUR resonance and their ability to generate good acoustophoresis of a quality fully comparable to that obtained in conventional silicon-glass devices.

In the analysis presented here, we have focused on acoustophoresis similar to the one obtained by the simple standing pressure half-wave resonance that focuses suspended particles in the vertical center plane. However, our method is not restricted to this particular type of resonances. It is straightforward to extend it to searching for whole-system resonances with other spatial structures simply by changing the figure of merit to one that reflects the wanted type of resonance. We believe that the whole-system-ultrasound-resonance principle presented in this paper has the potential of becoming an important design tool in the development of high-quality, all-polymer, acoustofluidic devices.

ACKNOWLEDGEMENTS

RM was supported by the People Programme (Marie Curie Actions) of the European Union's Seventh Framework Programme (FP7/2007-2013) under REA grant agreement no. 609405 (COFUNDPostdocDTU). We are grateful for the discussions on experimental realizations of our ideas that we have had with Pelle Ohlsson, Ola Jakobsson, and Torsten Freltoft from AcouSort AB, and with Thomas Laurell at Lund University.

-
- [1] A. Lenshof, C. Magnusson, and T. Laurell, Acoustofluidics 8: Applications in acoustophoresis in continuous flow microsystems, *Lab Chip* **12**, 1210 (2012).
- [2] M. Gedge and M. Hill, Acoustofluidics 17: Surface acoustic wave devices for particle manipulation, *Lab Chip* **12**, 2998 (2012).
- [3] E. K. Sackmann, A. L. Fulton, and D. J. Beebe, The present and future role of microfluidics in biomedical research, *Nature* **507**, 181 (2014).
- [4] T. Laurell and A. Lenshof, eds., *Microscale Acoustofluidics* (Royal Society of Chemistry, Cambridge, 2015).
- [5] M. Antfolk and T. Laurell, Continuous flow microfluidic separation and processing of rare cells and bioparticles found in blood - A review, *Anal. Chim. Acta* **965**, 9 (2017).
- [6] P. Thevoz, J. D. Adams, H. Shea, H. Bruus, and H. T. Soh, Acoustophoretic synchronization of mammalian cells in microchannels, *Anal. Chem.* **82**, 3094 (2010).
- [7] P. Augustsson, C. Magnusson, M. Nordin, H. Lilja, and T. Laurell, Microfluidic, label-free enrichment of prostate cancer cells in blood based on acoustophoresis, *Anal. Chem.* **84**, 7954 (2012).
- [8] R. Zmijan, U. S. Jonnalagadda, D. Carugo, Y. Kochi, E. Lemm, G. Packham, M. Hill, and P. Glynn-Jones, High throughput imaging cytometer with acoustic focusing, *RSC Advances* **5**, 83206 (2015).
- [9] M. Ohlin, I. Iranmanesh, A. E. Christakou, and M. Wiklund, Temperature-controlled mpa-pressure ultrasonic cell manipulation in a microfluidic chip, *Lab Chip* **15**, 3341 (2015).
- [10] D. J. Collins, B. Morahan, J. Garcia-Bustos, C. Doerig, M. Plebanski, and A. Neild, Two-dimensional single-cell patterning with one cell per well driven by surface acoustic waves, *Nat. Commun.* **6**, 8686 (2015).
- [11] F. Guo, Z. Mao, Y. Chen, Z. Xie, J. P. Lata, P. Li, L. Ren, J. Liu, J. Yang, M. Dao, S. Suresh, and T. J. Huang, Three-dimensional manipulation of single cells using surface acoustic waves, *PNAS* **113**, 1522 (2016).
- [12] P. Augustsson, J. T. Karlsen, H.-W. Su, H. Bruus, and J. Voldman, Iso-acoustic focusing of cells for size-insensitive acousto-mechanical phenotyping, *Nat. Commun.* **7**, 11556 (2016).
- [13] P. Ohlsson, M. Evander, K. Petersson, L. Mellhammar, A. Lehmusvuori, U. Karhunen, M. Soikkeli, T. Seppa, E. Tuunainen, A. Spangar, P. von Lode, K. Rantakokko-Jalava, G. Otto, S. Scheduling, T. Soukka, S. Wittfooth, and T. Laurell, Integrated acoustic separation, enrichment, and microchip polymerase chain reaction detection of bacteria from blood for rapid sepsis diagnostics, *Anal. Chem.* **88**, 9403 (2016).
- [14] B. Hammarström, B. Nilson, T. Laurell, J. Nilsson, and S. Ekström, Acoustic trapping for bacteria identification in positive blood cultures with maldi-tof ms, *Anal. Chem.* **86**, 10560 (2014).
- [15] G. Sitters, D. Kamsma, G. Thalhammer, M. Ritsch-Marte, E. J. G. Peterman, and G. J. L. Wuite, Acoustic force spectroscopy, *Nat. Meth.* **12**, 47 (2015).
- [16] B. W. Drinkwater, Dynamic-field devices for the ultrasonic manipulation of microparticles, *Lab Chip* **16**, 2360 (2016).
- [17] D. J. Collins, C. Devendran, Z. Ma, J. W. Ng, A. Neild, and Y. Ai, Acoustic tweezers via sub-time-of-flight regime surface acoustic waves, *Science Advances* **2**, e1600089 (2016).
- [18] H. G. Lim, Y. Li, M.-Y. Lin, C. Yoon, C. Lee, H. Jung, R. H. Chow, and K. K. Shung, Calibration of trapping force on cell-size objects from ultrahigh-frequency single-beam acoustic tweezer, *IEEE T. Ultrason. Ferr.* **63**, 1988 (2016).
- [19] D. Baresch, J.-L. Thomas, and R. Marchiano, Observation of a single-beam gradient force acoustical trap for elastic particles: Acoustical tweezers, *Phys. Rev. Lett.* **116**, 024301 (2016).
- [20] G. P. Gautam, T. Burger, A. Wilcox, M. J. Cumbo, S. W. Graves, and M. E. Piyasena, Simple and inexpensive micromachined aluminum microfluidic devices for acoustic focusing of particles and cells, *Anal. Bioanal. Chem.* **410**, 3385 (2018).
- [21] A. Fornell, K. Cushing, J. Nilsson, and M. Tenje, Binary particle separation in droplet microfluidics using acoustophoresis, *Appl. Phys. Lett.* **112**, 063701 (2018).
- [22] K. Petersson, O. Jakobsson, P. Ohlsson, P. Augustsson, S. Scheduling, J. Malm, and T. Laurell, Acoustofluidic hematocrit determination, *Anal. Chim. Acta* **1000**, 199 (2018).
- [23] C. Magnusson, P. Augustsson, A. Lenshof, Y. Ceder, T. Laurell, and H. Lilja, Clinical-scale cell-surface-marker independent acoustic microfluidic enrichment of tumor cells from blood, *Anal. Chem.* **89**, 11954 (2017).
- [24] D. Ahmed, A. Ozcelik, N. Bojanala, N. Nama, A. Upadhyay, Y. Chen, W. Hanna-Rose, and T. J. Huang, Rotational manipulation of single cells and organisms using acoustic waves, *Nat. Commun.* **7**, 11085 (2016).
- [25] W. Zhou, J. Wang, K. Wang, B. Huang, L. Niu, F. Li, F. Cai, Y. Chen, X. Liu, X. Zhang, H. Cheng, L. Kang, L. Meng, and H. Zheng, Ultrasound neuro-modulation chip: activation of sensory neurons in caenorhabditis elegans by surface acoustic waves, *Lab Chip* **17**, 1725 (2017).
- [26] P. Sehgal and B. J. Kirby, Separation of 300 and 100 nm particles in fabry-perot acoustofluidic resonators, *Anal. Chem.* **89**, 12192 (2017).
- [27] M. Wu, Z. Mao, K. Chen, H. Bachman, Y. Chen, J. Rufo, L. Ren, P. Li, L. Wang, and T. J. Huang, Acoustic separation of nanoparticles in continuous flow, *Adv. Funct. Mater.* **27**, 1606039 (2017).
- [28] D. J. Collins, R. O'Rourke, C. Devendran, Z. Ma, J. Han, A. Neild, and Y. Ai, Self-aligned acoustofluidic particle focusing and patterning in microfluidic channels from channel-based acoustic waveguides, *Phys. Rev. Lett.* **120**, 074502 (2018).
- [29] W. L. Ung, K. Mutafooulos, P. Spink, R. W. Rambach, T. Franke, and D. A. Weitz, Enhanced surface acoustic wave cell sorting by 3d microfluidic-chip design, *Lab Chip* **17**, 4059 (2017).
- [30] K. Park, J. Park, J. H. Jung, H. Ahmed, and H. J. Sung, In-droplet microparticle separation using travelling surface acoustic wave, *Biomicrofluidics* **11**, 064112 (2017).
- [31] B. J. Kim and E. Meng, Review of polymer MEMS micromachining, *J. Micromech. Microeng.* **26**, 013001 (2016).

- [32] N. Harris, M. Hill, A. Keating, and P. Baylac-Choulet, A lateral mode flow-through PMMA ultrasonic separator, *Intl. J. Appl. Biomed. Eng.* **5**, 20 (2012).
- [33] A. Mueller, A. Lever, T. V. Nguyen, J. Comolli, and J. Fiering, Continuous acoustic separation in a thermoplastic microchannel, *J Micromech Microeng* **23**, 125006 (2013).
- [34] I. Gonzalez, M. Tijero, A. Martin, V. Acosta, J. Berganzo, A. Castillejo, M. M. Bouali, and J. Luis Soto, Optimizing polymer lab-on-chip platforms for ultrasonic manipulation: Influence of the substrate, *Micromachines* **6**, 574 (2015).
- [35] C. Yang, Z. Li, P. Li, W. Shao, P. Bai, and Y. Cui, Acoustic particle sorting by integrated micromachined ultrasound transducers on polymerbased microchips, *IEEE International Ultrasonics Symposium (IUS)*.
- [36] W. J. Savage, J. R. Burns, and J. Fiering, Safety of acoustic separation in plastic devices for extracorporeal blood processing, *Transfusion* **57**, 1818 (2017).
- [37] R. Silva, P. Dow, R. Dubay, C. Lissandrello, J. Holder, D. Densmore, and J. Fiering, Rapid prototyping and parametric optimization of plastic acoustofluidic devices for blood-bacteria separation, *Biomedical Microdevices* **19**, 70 (2017).
- [38] C. Lissandrello, R. Dubay, K. T. Kotz, and J. Fiering, Purification of lymphocytes by acoustic separation in plastic microchannels, *SLAS Technology* **23**, 352 (2018).
- [39] P. B. Muller, R. Barnkob, M. J. H. Jensen, and H. Bruus, A numerical study of microparticle acoustophoresis driven by acoustic radiation forces and streaming-induced drag forces, *Lab Chip* **12**, 4617 (2012).
- [40] P. B. Muller and H. Bruus, Numerical study of thermoviscous effects in ultrasound-induced acoustic streaming in microchannels, *Phys. Rev. E* **90**, 043016 (2014).
- [41] P. B. Muller and H. Bruus, Theoretical study of time-dependent, ultrasound-induced acoustic streaming in microchannels, *Phys. Rev. E* **92**, 063018 (2015).
- [42] J. S. Bach and H. Bruus, Theory of pressure acoustics with viscous boundary layers and streaming in curved elastic cavities, *J. Acoust. Soc. Am.* **144**, 766 (2018).
- [43] R. Barnkob, P. Augustsson, T. Laurell, and H. Bruus, Measuring the local pressure amplitude in microchannel acoustophoresis, *Lab Chip* **10**, 563 (2010).
- [44] P. Augustsson, R. Barnkob, S. T. Wereley, H. Bruus, and T. Laurell, Automated and temperature-controlled micro-piv measurements enabling long-term-stable microchannel acoustophoresis characterization, *Lab Chip* **11**, 4152 (2011).
- [45] R. Barnkob, P. Augustsson, T. Laurell, and H. Bruus, Acoustic radiation- and streaming-induced microparticle velocities determined by microparticle image velocimetry in an ultrasound symmetry plane, *Phys. Rev. E* **86**, 056307 (2012).
- [46] P. B. Muller, M. Rossi, A. G. Marin, R. Barnkob, P. Augustsson, T. Laurell, C. J. Kähler, and H. Bruus, Ultrasound-induced acoustophoretic motion of microparticles in three dimensions, *Phys. Rev. E* **88**, 023006 (2013).
- [47] H. Sutherland and R. Lingle, Acoustic characterization of polymethyl methacrylate and 3 epoxy formulations, *J. Appl. Phys.* **43**, 4022 (1972).
- [48] H. Sutherland, Acoustical determination of shear relaxation functions for polymethyl methacrylate and Epon 828-Z, *J. Appl. Phys.* **49**, 3941 (1978).
- [49] J. E. Carlson, J. van Deventer, A. Scolan, and C. Carlander, Frequency and temperature dependence of acoustic properties of polymers used in pulse-echo systems, *2003 IEEE Symposium on Ultrasonics*, 885 (2003).
- [50] P. H. Mott, J. R. Dorgan, and C. M. Roland, The bulk modulus and poisson's ratio of "incompressible" materials, *J Sound Vibr* **312**, 572 (2008).
- [51] P. Adler, Novel materials and designs for cell separation by acoustofluidics, in *Master's thesis* (2014).
- [52] S. Kasarova, N. Sultanova, and I. Nikolov, Polymer materials in optical design, *Bulgarian Chemical Communications* **47**, 44 (2015).
- [53] *Glass Silicon Constraint Substrates*, CORNING, Houghton Park C-8, Corning, NY 14831, USA, <http://www.valleydesign.com/Datasheets/Corning%20Pyrex%207740.pdf>, accessed 11 November 2016.
- [54] M. A. Hopcroft, W. D. Nix, and T. W. Kenny, What is the Young's modulus of silicon, *J. Microelectromech. Syst* **19**, 229 (2010).
- [55] P. Hahn and J. Dual, A numerically efficient damping model for acoustic resonances in microfluidic cavities, *Phys. Fluids* **27**, 062005 (2015).
- [56] B. Hartmann and J. Jarzynski, Polymer sound speeds and elastic constants, Naval Ordnance Laboratory, Report NOLTR **72-269**, 1 (1972), <http://www.dtic.mil/dtic/tr/fulltext/u2/755695.pdf>, accessed 16 August 2018.
- [57] J. T. Karlsen and H. Bruus, Forces acting on a small particle in an acoustical field in a thermoviscous fluid, *Phys. Rev. E* **92**, 043010 (2015).
- [58] L. D. Landau and E. M. Lifshitz, *Theory of Elasticity. Course of Theoretical Physics*, 3rd ed., Vol. 7 (Pergamon Press, Oxford, 1986).
- [59] M. W. H. Ley and H. Bruus, Three-dimensional numerical modeling of acoustic trapping in glass capillaries, *Phys. Rev. Applied* **8**, 024020 (2017).
- [60] J. Dual and T. Schwarz, Acoustofluidics 3: Continuum mechanics for ultrasonic particle manipulation, *Lab Chip* **12**, 244 (2012).
- [61] M. Settnes and H. Bruus, Forces acting on a small particle in an acoustical field in a viscous fluid, *Phys. Rev. E* **85**, 016327 (2012).
- [62] COMSOL Multiphysics 5.3a, www.comsol.com (2017).
- [63] AcouSort AB, www.acousort.com, private communication, 2018.